Direct dating of 3.5 Ga biogenic carbon in a microbial mat remnant, Singhbhum Craton, India

Trisrota Chaudhuri, T. Mark Harrison, Elizabeth A. Bell, Mark Van Zuilen, Léna Thomas, Nouf Al Alawi, Rajat Mazumder, and Stefan V. Lalonde

Direct dating of 3.5 Ga biogenic carbon in a microbial mat remnant, Singhbhum Craton, India

Trisrota Chaudhuri[a,1], T. Mark Harrison[b,1], Elizabeth A. Bell[b], Mark Van Zuilen[c], Léna Thomas[d], Nouf Al Alawi[e], Rajat Mazumder[e,f], and Stefan V. Lalonde[g]

Affiliations are included on p. 8.

Contributed by T. Mark Harrison; received May 22, 2026; accepted June 19, 2026; reviewed by Christopher H. House and Stephen J. Mojzsis

Zircons interpreted to be of syn-volcanic origin recovered from the lower greenschist "black and white banded" Bhitardari chert, Eastern Iron Ore greenstone belt, Singhbhum craton, India, yield a $^{207}Pb/^{206}Pb$ zircon age of 3497 ± 5 Ma (n = 4; MSWD = 1.2). This chert contains abundant carbonaceous matter (CM) that occurs in two textural modes: 1) ultrafine laminae distributed within the matrix and 2) graphite flakes in late quartz veins. Bulk $\delta^{13}C_{CM}$ of both modes in the Bhitardari chert yield a value of −30.9‰, which we interpret as reflecting a biogenic origin. This represents the documentation of a directly dated, CM-bearing, Paleoarchean rock with $\delta^{13}C_{CM}$ diagnostic of biologic activity. The observed isotopic compositions are consistent with the rise of relatively sophisticated metabolic mechanisms (e.g., Calvin cycle) by 3.5 Ga.

kerogen | zircon | early life

Significance

Kerogen, insoluble organic matter preserved in sediments, represents some of the earliest known terrestrial biosignatures which have provided important insights into the origin of life and planetary habitability. Direct dating of these materials can be complicated by the lack of suitable geochronometers, instead relying on indirect constraints from, for example, the age of cross cutting lithologies. Here, we report a 3.5-billion-year-old carbonaceous chert from eastern India containing what are interpreted to be contemporaneous tuffaceous zircons. The chert exhibits micron-scale alternating layers of carbonaceous and siliceous materials. $\delta^{13}C$ isotope data of carbonaceous matter (CM) together with stratigraphic relationships indicate a biogenic origin of the kerogen marking this to our knowledge the oldest directly dated rock with a confirmed biosignature.

Early microbial traces are found in predominantly marine and hydrothermal environments in the form of residual carbonaceous matter, biominerals, microbial mats, and stromatolites [(1–5) and references therein]. It is important to identify the earliest biosignatures to understand the complex process of initiation of life on Earth. Paleorchean chemogenic sediments, especially cherts hold rare archives of the earliest biosphere as rapid silica precipitation entombed syngenetic organic matter (OM) within physically and chemically inert silica matrices, retaining kerogen textures, carbon isotopic signatures, and molecule-level organization despite multiple postdepositional geologic processes over time (6–10). Their intimate association with hydrothermal–greenstone successions and BIF-bearing sedimentary systems further links early carbon cycling and microbial activity to Archean volcanic–oceanic environments (10, 11).

Paleoarchean black cherts and volcanic–sedimentary successions preserve isotopically light carbonaceous matter (CM) and putative microbial structures. Microbially induced sedimentary structures (MISS; 12) from 3480 Ma black chert breccias of the Barberton Greenstone Belt yield $\delta^{13}C$ values between −25‰ and −29.5‰ (13, 14). Putative stromatolites have been reported from the ca. 3709 Ma Isua supracrustal belt (11) the 3430 Ma Strelley Pool Formation (15, 16 and references therein), the c. 3500 Ma bedded barite from Dresser Formation, Pilbara Craton (17, 18), the c. 3550 to 3230 Ma Barberton Greenstone Belt (1, 19, 20), and the c. 3200 Ma Moodies Group, South Africa (21). However, the "stromatolite-like" structures in the ISB appears better interpreted as a tectonic fabric, i.e., folding of compositional planes rather than biogenic structures formed in chemogenic metasediments (22, 23). Some of the oldest and most significant occurrences of CM were reported from the ca. 3.7 to 3.8 Ga Isua supracrustal belt, southwestern Greenland, where graphite particles hosted in metasediments yield $\delta^{13}C$ values as low as −24‰, consistent with biological carbon fixation (24–26 and references therein). Locally elevated $\delta^{13}C$ values up to −6‰ were attributed to partial isotopic equilibration with carbonate and/or CO_2-bearing metamorphic fluids during amphibolite-facies metamorphism (24). Moreover, graphite formed by siderite breakdown in metacarbonate veins also shows comparatively less negative isotopic compositions (27, 28). Graphite inclusions in apatite from ≥3.83 Ga Fe-rich metasediments on Akilia Island exhibit even lighter $\delta^{13}C$ values of −37‰, suggestive of a biogenic precursor (29–31). Two parallel studies propose graphite formation through secondary CO_2–CH_4 fluid deposition during metamorphism from either biogenic and/or inorganic carbon sources (32, 33). Nevertheless, an additional process is required to explain the extremely negative $\delta^{13}C$ signatures recorded by graphite from the ISB and Akilia rocks.

Preservation of Paleoarchean microbial mats is rare due to subsequent deformation and metamorphism. Thus, careful identification is required as abiotic processes may generate "biomarker-like" signatures (6, 34–37, and references therein). High-resolution Raman

Author contributions: T.C., T.M.H., E.A.B., M.V.Z., and R.M. designed research; T.C., E.A.B., L.T., and S.V.L. performed research; T.C., T.M.H., E.A.B., M.V.Z., L.T., N.A.A., R.M., and S.V.L. analyzed data; and T.C., T.M.H., E.A.B., M.V.Z., and R.M. wrote the paper.

Reviewers: C.H.H., The Pennsylvania State University; and S.J.M., Universitat Bayreuth Bayerisches Forschungsinstitut fur Experimentelle Geochemie und Geophysik.

The authors declare no competing interest.

[1]To whom correspondence may be addressed. Email: trisrota.chaudhuri@gsi.gov.in or tmh@epss.ucla.edu.

This article contains supporting information online at https://www.pnas.org/lookup/suppl/doi:10.1073/pnas.2617912123/-/DCSupplemental.

Published August 17, 2026.

spectroscopic analyses provide a critical means of syngenicity testing of carbonaceous matter (CM) by resolving D–G band characteristics, structural order–disorder, and thermal maturity, thereby discriminating syngenetic CM–a fraction that was initially incorporated in the host rock and experienced the same peak metamorphism–from later introduced fractions such as recent organic contamination. Furthermore, Raman analysis enables detection of spatial variations in CM structural order, resulting from local shearing and/or hydrothermal fluid circulation. Raman spectroscopic characteristics for syngenicity testing along with biogenic morphological features, $\delta^{13}C$ signature together can establish a robust framework for assessing the biogenicity and preservation history of Paleoarchean carbonaceous material (38–40).

The Singhbhum Craton, eastern India, preserves one of the oldest records of continental crust formation, with its growth initiated in the Hadean (ca. 4.2 to 4.0 Ga; 41) that reached a peak at ca. 3.3 Ga (42). Previous reports of Paleoarchean cherts from the Eastern and Southern Iron Ore Greenstone Belts containing carbonaceous matter (CM) of possible biogenic origin (43–45) were associated with felsic tuff dated at (3510 Ma; 44). However, direct temporal constraints coupled with an integrated, multiproxy approach to robustly establish biogenicity of CM from the same lithology have not been previously obtained. Here, we integrate in situ U–Pb zircon geochronology, $^{13}C/^{12}C$ and $^{15}N/^{14}N$ isotope compositions, and Raman spectroscopic characterization of kerogen-hosted CM from a "black-and-white" banded chert associated with banded iron formation (BIF) at the northern margin of the Eastern Iron Ore Greenstone Belt. The CM-bearing chert is interlayered with siliceous and carbonaceous phyllite, discrete BIF bands, and localized chert-pebble conglomerate, providing a well-constrained stratigraphic context.

In this report, we establish a direct temporal association between CM and its depositional framework and apply a multiproxy analytical approach to evaluate its origin.

1.1 Regional Geology. The Eastern Iron Ore Group (IOG), also referred to as the Gorumahishani Greenstone Belt, forms part of the eastern Singhbhum cratonic nucleus (Fig. 1*A*). The belt extends for ~120 km, trending NNW–SSE in its northern segment, transitioning to a near N–S orientation centrally, and bifurcating southward into a fork-like geometry (Fig. 1*A*). Its width varies from ~5 km near Aunlajhori to ~25 km near Potka. The stratigraphic succession of this greenstone belt comprises a thick assemblage of mafic–ultramafic rocks with subordinate felsic volcanic and volcaniclastic units, interlayered with detrital and chemical sedimentary rocks (Fig. 1*B*).

A major iron ore deposit occurs south of Badampahar, developed above an approximately 200-m-thick banded iron formation (BIF; 46) The northern segment of the belt is dominated by deformed, lower amphibolite-facies volcanic and volcaniclastic rocks, chert, and siliciclastic sediments, with only minor and discontinuous BIF occurrences (46). The IOG succession records polyphase deformation and is organized into a regional anticlinorium with a WNW–ESE–striking axial plane (46). This structure is overturned toward the southwest, with a gently dipping northern limb and a steep southern limb (46). The dominant fold architecture corresponds to second-generation (F_2) structures that are coaxial with earlier F_1 folds and become reclined toward the Singhbhum Shear Zone. Later F_3 deformation produced broad warps with axial planes, oriented transverse to the pervasive foliation. The oldest age constraint for the eastern IOG is 3510 Ma, derived from felsic volcaniclastic rocks associated with carbonaceous chert from the supracrustal association, near Udal and Kundarkocha villages (43), located south of the present study area (Fig. 1*A*).

1.2 Local Geology and Field Observations. The study area lies in the northern extremity of the eastern IOG greenstone belt where it turns nearly E-W against the regional, Singhbhum Shear Zone of Paleoproterozoic age (Fig. 1*A*). The lithology of the area is a part of WNW-ESE striking tight fold, overturned toward north (46). The lithological sequence is defined by parallel bands of banded black-and-white chert (Fig. 2 *A* and *B*), BIF (Fig. 2*C*), sheared quartz-pebble conglomerate (Fig. 2*D*), chert-pebble conglomerate (Fig. 2*E*), phyllite (Fig. 2*F*). The entire succession is folded into two successive phases of folding (F_1 and F_2) followed by F_3 broad warps ((47); Dataset S1). Primary bedding planes in recrystallized quartzite, phyllite, and compositional banding in chert and BIF are tightly folded into two successive phases of deformations. The strike of the bedding plane and the pervasive foliation are subparallel along N55°W-S55°E dipping 35°–45° toward NE (Dataset S1).

The pervasive WNW-ESE foliation is evident in all rocks including the matrix of the conglomerate. Intermittent lenticular bodies of chert and quartz clast conglomerates are present along the contacts between the chert, phyllite, and quartz phyllite- (Dataset S1). The conglomerate clasts are stretched toward down-dip direction (N30°–40°E; Fig. 2*D*). The entire phyllite-chert package grades into a slaty phyllite-quartzite sequence toward north. The last phase of deformation is recorded by a discreet foliation striking along N10°E-S10°W. The volcano-sedimentary sequence belongs to the northern part of the Paleoarchean Eastern IOG greenstone basin. The carbonaceous chert horizon of Bhitardari occurs as an NW-SE trending band parallel to the general strike (N55°W) of the litho-units. The outcrop of the chert is cut across by numerous quartz veins of different generations. Quartz veins along with the primary banding exhibit tight, reclined folding with axial plane N50°W/45°NE. Stretching lineations of quartz are aligned parallel to the fold axis (42°→40°). The fold hinges defined by quartz veins are sometimes thickened and detached from the limbs (Fig. 2*B*).

1.3 Petrography. Thin sections of CM-bearing cherts exhibit rhythmic, submillimeter-scale laminations alternating between quartz-rich and carbonaceous material (CM)-rich layers (Fig. 3*A*). Under plane-polarized light, their appearance varies with the relative quartz–CM ratio (Fig. 3*B*). Quartz grains are commonly microcrystalline with polygonal boundaries although microdomains showing relict cryptocrystalline texture are still preserved. Primary laminations are frequently crosscut by later quartz veins with polygonal boundaries and coarser graphitic flakes (Fig. 3*B*). Extensional, quartz-filled veinlets traverse across the primary quartz-CM laminations (Fig. 3*C*). Associated gray phyllite shows embayed and bipyramidal quartz clasts indicating that they might be volcanic in origin (Fig. 3*D*). Apatite and zircon grains are more visible in quartz-rich microdomains (Fig. 3*E*).

2. Results

2.1. Raman Spectroscopy. Raman spectroscopic analyses reveal two structurally distinct carbon populations within sample BTDR1. Matrix-hosted CM occurs as dispersed particles and exhibits a relatively low degree of structural ordering consistent with lower greenschist-facies metamorphism. Representative spectra are characterized by a prominent D1 band near ~1,350 cm^{-1} with intensity exceeding that of the G band at ~1,580 cm^{-1}, together with a subordinate D2 shoulder near ~1,620 cm^{-1} (Fig. 3*F*). The matrix CM has high R1 values (~2.0 to 2.7) and R2 values (~0.6 to 0.75), corresponding to estimated peak temperatures of ~324 to 349 °C, except two higher values of 354 and 369 °C (Fig. 3 *G* and *H*). Depth-profile Raman analyses comparing

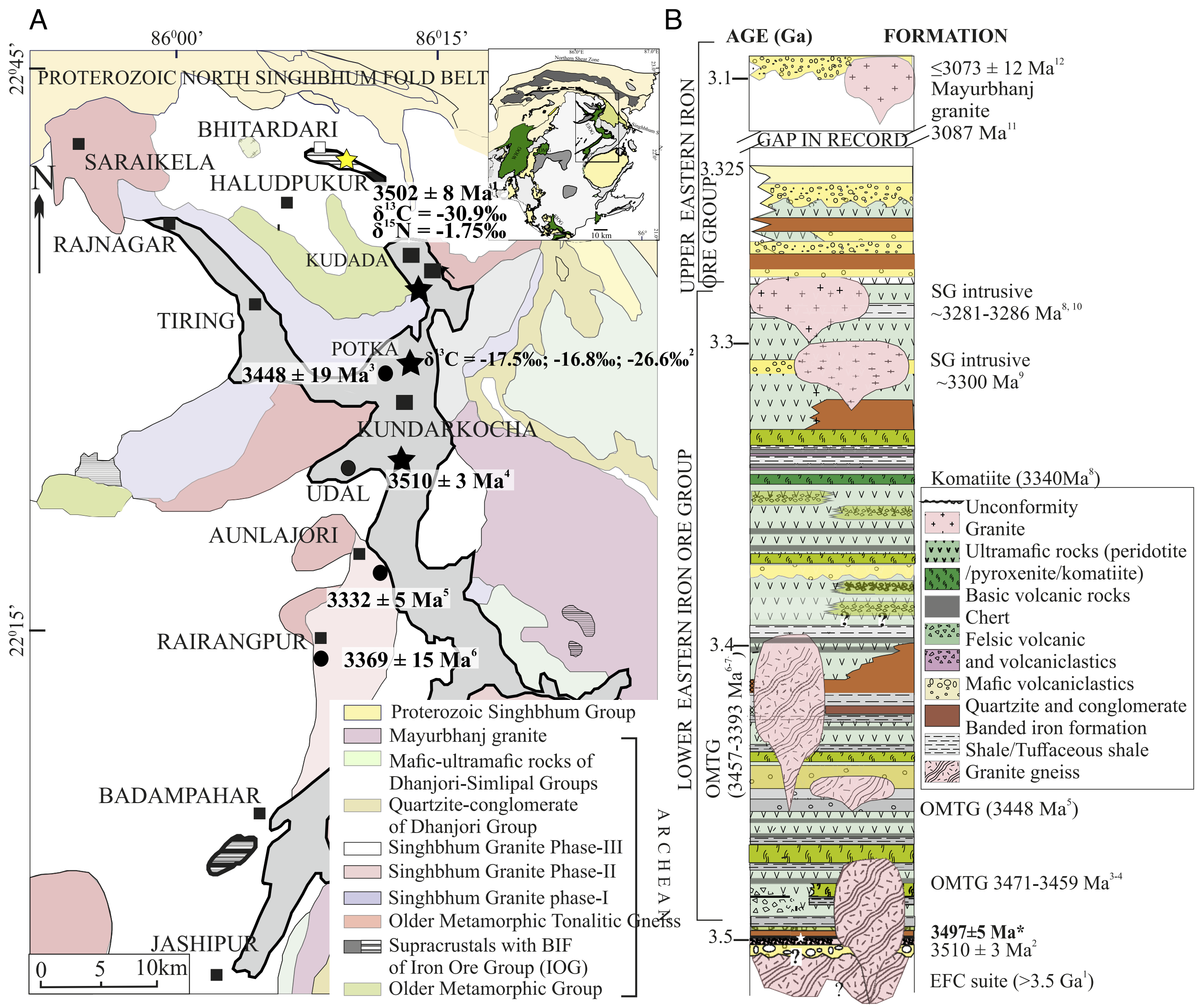

Fig. 1. (*A*) Geological map of the Eastern Iron Group (geological map of the Singhbhum craton in inset both modified after Dunn & Dey, 46) showing locations of previously reported carbonaceous chert (black star), U-Pb zircon age of intrusive granite (black circle), felsic volcanic rock (white circle), Bhitardari chert (yellow star); see more details in Table 1. (*B*) Time-integrated litho-stratigraphy of the eastern Iron Ore Group (EIOG). Abbreviations: EFC: Early Felsic Crust, OMTG: Older Metamorphic Tonalitic Gneiss, SG: Singhbhum Granitoid suite. Superscripts represent reference articles of the corresponding age and isotope data summarized in *SI Appendix*.

surface and deeper laser penetration levels show closely overlapping R1 (~1.8 to 2.8) and R2 (~0.55 to 0.75) distributions (Dataset S2). Surface measurements display slightly higher R1 values relative to deeper analyses, indicating marginally greater disorder near the surface; however, both datasets occupy the same broad compositional field eliminating the effects of polishing-induced artifact. The average R2-derived peak temperature for the matrix-hosted CM for surface and deeper analysis are identical, viz. 337 ± 8 °C and 336 ± 8 °C (Dataset S2). Notably, we report a precise average temperature of 338 ± 9 °C of the surface and depth analyses with much less uncertainty than the geothermometer by Beysaac et al. (38; i.e., ±50 °C).

Raman spectra of the vein-hosted flaky CM display very weak or nearly absent D1 bands and well-formed G-peak, indicating advanced structural ordering. Two analyses (spectra 17 and 24) show anomalously higher disorder and may reflect polishing-induced artifacts. Excluding these analyses, the vein-hosted CM yields a large range of R2-derived peak temperature i.e., 528 to 639 with an average of 596 ± 36 °C; inclusion of all analyses gives an average of 544 ± 114 °C (Fig. 3 *G* and *H*).

2.2. U-Pb Age of the CM-Bearing Chert. Out of the eight zircons analyzed, four are between 11 to 129% discordant while four yield concordant $^{207}Pb/^{206}Pb$ ages of 3471 ± 8 Ma, 3492 ± 7 Ma, 3498 ± 3 Ma and 3510 ± 5 Ma (Table 2; Dataset S3) with a weighted mean age of 3497 ± 5 Ma (2 SE, MSWD: 1.2). Th/U for these spots vary between 0.33 and 0.81 supporting a magmatic origin. The discordant zircons define an array with an upper concordia intercept of 3.5 Ga and a lower intercept age of ~ 850 Ma (Fig. 4*A*). All the zircons exhibit oscillatory zoning in CL and are ~40 to 60 μm in size in the longer axis (Fig. 4 *B–G*). Among the discordant zircons, the level of discordance increases with U concentration, suggesting that accumulation of radiation damage enhanced Pb loss during a later event, likely through the progressive amorphization of the zircon crystal lattice (e.g., ref. 48).

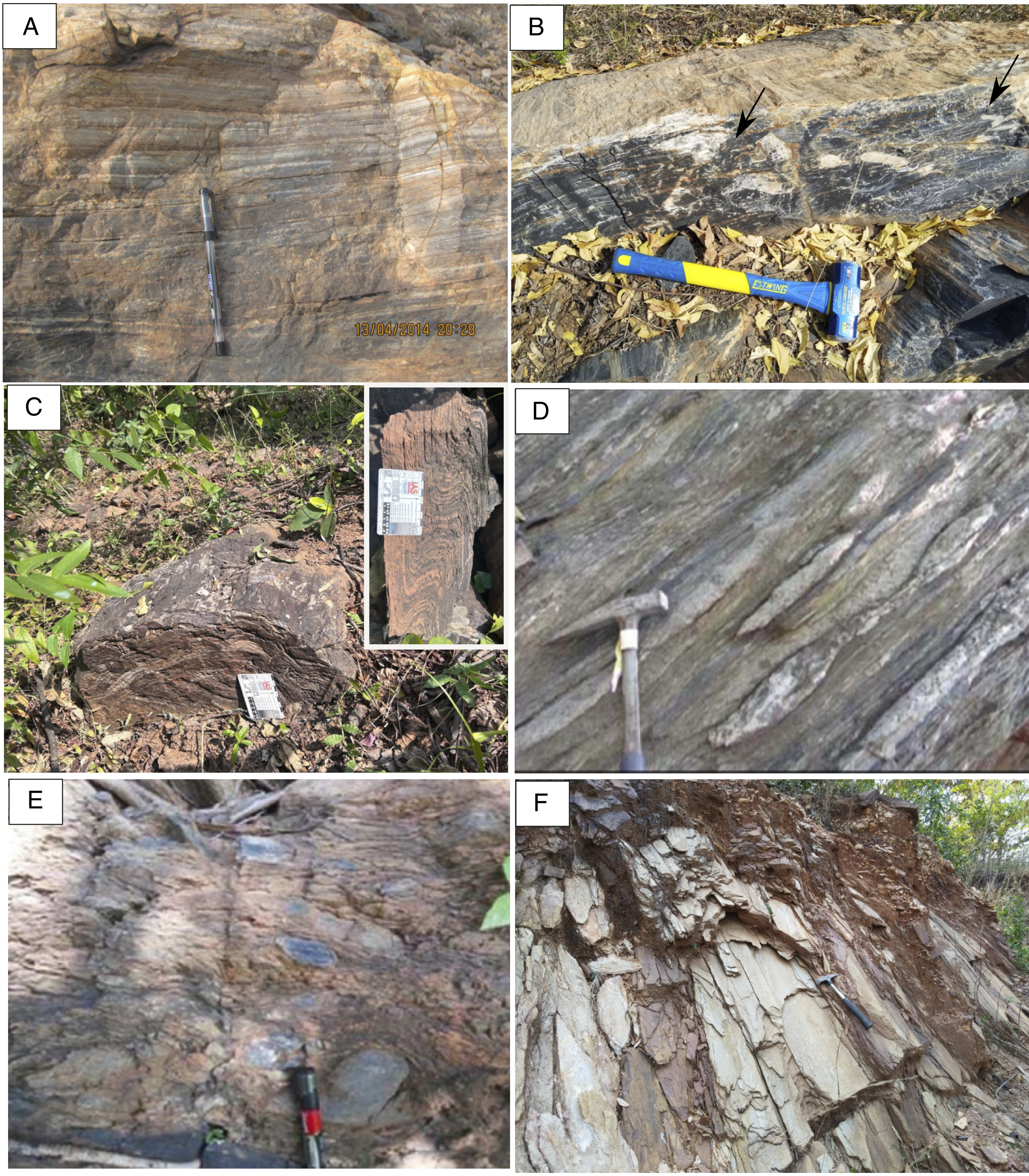

Fig. 2. (*A*) Outcrop photo of carbonaceous chert; (*B*) Hinge of reclined fold (F1; black arrow) of the primary compositional banding (and bedding-parallel quartz vein) and down-plunging stretching lineations parallel to the fold axis. (*C*) Outcrop of BIF (22°41′50.7″ N; 86°09′57.9″ E) associated with carbonaceous chert; (*Inset*) close-view of BIF showing tight, vertical fold (*D*) Stretched quartz clasts in deformed conglomerate associated with quartzite and carbonaceous chert. (*E*) deformed phyllite above the chert horizon with rip-up clasts of banded carbonaceous chert. (*F*) deformed quartz phyllite associated with carbonaceous chert and chert-pebble horizon. (*D* and *E*) are after Das et al. (47).

2.3. C- and N Isotope Analysis. HF-treated sample of BTDR-1 yields a $\delta^{13}C_{org}$ value of −30.92‰ while the HCl-treated sample yields a $\delta^{13}C_{org}$ value of −27.17‰ This difference clearly shows that some carbonate fraction was retained after only HCl treatment, causing an upward shift in ^{13}C. The observed $\delta^{15}N_{org}$ is −1.8%, but the concentration of N was too low to make this a reliable observation. We therefore refrain from interpreting the $\delta^{15}N_{org}$ of the CM in BTDR-1. Detailed results of standard and analyses are furnished in the Dataset S4.

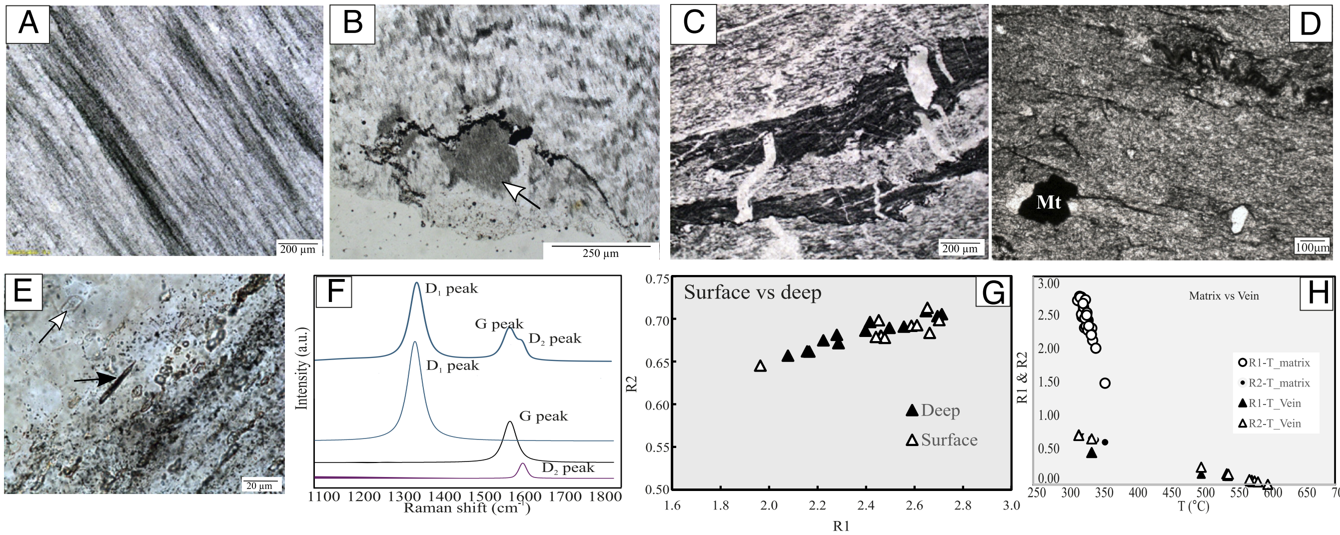

Fig. 3. Photomicrographs showing (*A*) Alternate CM and quartz-rich banding, (*B*) Primary quartz and CM-bearing lamination (white arrow) cut across by quartz vein with graphite flakes, (*C*) quartz-filled tension gashes across carbonaceous lamination, (*D*) quartz clasts within tuffaceous phyllite with fine-carbonaceous material in the matrix, (*E*) Zircon (black arrow) and apatite (white arrow) within carbonaceous chert, (*F*) Raman spectra of CM showing all (above) and individual (below) peak positions, (*G*) Temperature (°C) vs. R1 and R2 ratio plots of Raman analyses of CM within matrix (n = 36) and vein (n = 10), (*H*) Temperature (°C) vs. D1 and G positions of Raman analyses of matrix CM.

3. Discussion

3.1. Preservation Potential of Organic Matter (OM) in Bhitardari Chert. Raman spectra of the matrix CM are dominated by a broad D1 band (~1,350 cm^{-1}), a G band (~1,580 cm^{-1}), and a subordinate D2 shoulder (~1,620 cm^{-1}). The prominence of the D1 band relative to the G band in the matrix-hosted CM indicates preservation of structural disorder or incomplete graphitization, characteristic of metamorphosed kerogen (38, 49). Matrix-hosted carbon displays high R1 (~2.0 to 2.7) and R2 (~0.6 to 0.75) ratios. Applying the geothermometer of Beyssac et al. (38; see *Materials and Methods*) results in a temperature range of 324 to 369 °C (average 338 ± 8.7 °C; n = 34). These values are consistent with lower greenschist-facies metamorphism and indicate that the CM retained substantial structural disorder despite prolonged geological evolution. In contrast, vein-hosted carbon exhibits very low R1 and R2 values and significantly higher calculated temperatures (~520 to 650 °C), reflecting advanced graphitic ordering produced during localized high-temperature recrystallization. The sharp separation between matrix and vein populations demonstrates that Raman parameters sensitively record distinct carbon transformation pathways within the same rock and they corroborate with the optical characters as well.

The temperature estimates derived from Raman geothermometry are particularly important because they provide an independent constraint on the metamorphic evolution of the CM. Raman-based peak temperatures reflect the maximum structural ordering attained by carbonaceous matter during metamorphism and are therefore valuable indicators of thermal maturity (38). The lower temperatures recorded by the matrix CM imply that the original kerogenous material was never fully equilibrated with the quartz-graphite veins corresponding to later thermal activity. Instead, graphitization was spatially restricted to fluid pathways where enhanced heat transfer, deformation, and fluid-assisted dissolution–reprecipitation accelerated structural reorganization of carbon (50). To exclude polishing-induced structural disordering, Raman measurements were acquired from both surface and deeper analytical levels (Dataset S2). The closely overlapping R1–R2 distributions indicate that the observed disorder is intrinsic to the carbonaceous matter rather than a surface artifact caused by polishing, oxidation, or contamination. Likewise, the narrow clustering of D1 and G peak positions reflects a relatively homogeneous structural organization within the matrix-hosted CM population.

Collectively, the Raman data indicate preservation of syngenetic, poorly ordered Archean kerogen within the siliceous matrix, subsequently overprinted by localized hydrothermal graphitization along veins.

Table 1. Records of CM-bearing chert from EIOG greenstone belt

Sl No	Area and rock type	Age (Ma)	Location (coordinates)	Temperature (°C) from Raman peak of CM	δ^{13}C(‰; CM)	Reference
1	Kunderkocha; Brecciated carbonaceous chert	Not dated	22°27′ 11″ N 86°14′ 19″ E	423 and 460 (±50) °C.	–	(43)
2	Udal (Felsic volcaniclastic rock and intercalated carbonaceous chert (granular and bedded)	3510 ± 6 Ma	22°32′ 43″N 86°16′ 31″ E	450 and 475 (±50) °C,	–	(43)
3	Potka (carbonaceous chert)	>3,448 ± 19 Ma; Age of intrusive TTG	22°36′34″N 86°13′15″E	450 (±50) °C (n = 2) 519 (±50) °C (n = 1)	−17.5‰ (RT-2) −16.8‰ (RT-3) −6.6‰ (RT-7)	(45)
4	Bhitardari (carbonaceous chert)	3,502.3 ± 7.6 Ma	22°41′30.9″N 86°10′41.1″E	338 ± 9 °C	−30.92‰ (δ^{13}C); −1.75‰ (δ^{15}N)	This study

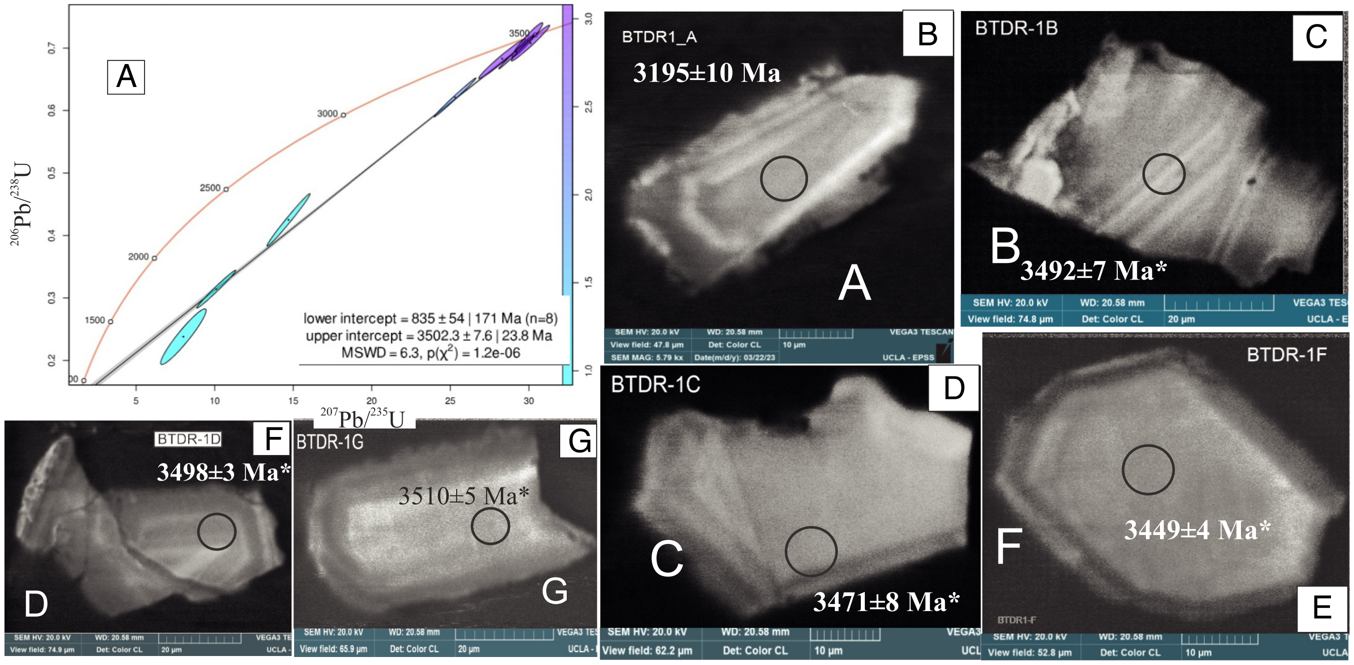

Fig. 4. (*A*) U-Pb concordia diagram of analyses spots of zircon from sample BTDR-1. (*B*–*G*) Cathodoluminescence (CL) images of zircon showing spot ages.

3.2. Age and Depositional Condition of Bhitardari Carbonaceous Chert, Singhbhum Craton. Recovery and dating of zircons from Precambrian cherts is exceptionally rare because these rocks generally contain little volcanic or detrital material and zircons are typically very small. The carbonaceous matter (CM)–bearing chert from Bhitardari in the Eastern Iron Ore Group (IOG) occurs with phyllite and discrete lensoidal banded iron formation (BIF). The enclosing phyllites contain embayed, cuspate, and lobate quartz grains indicating that they were tuffaceous in origin (Fig. 3*D*; 47). These phyllites also contain carbonaceous material identifiable under a microscope (Fig. 3*D*). Regional chert precipitation was likely driven by silica-rich hydrothermal fluids (51). From the fine-grained (40 to 60 µm), and elongated zircon morphology, oscillatory zoning in CL image and close association with tuffaceous metasediments and BIF, we propose that chemogenic sedimentation continued with volcanism and the zircons recovered from BTDR-1 chert are contemporaneous volcanic detritus. The interpreted zircon age of 3497 ± 5 Ma is consistent with the age of felsic tuff (3510 Ma) associated with carbonaceous cherts with kerogenous material from the stratigraphically equivalent horizon that was recovered from the central part of the greenstone belt (43; Fig. 1*A*).

Preservation of graphitic flakes formed at higher temperatures while the surrounding groundmass retains a disordered carbon structure may appear paradoxical. However, the occurrence of graphitic flakes within late hydrothermal veins cross-cutting the primary laminations is consistent with the highly localized nature of graphitization processes. Beyond temperature, graphitization is strongly influenced by fluid availability, permeability pathways, deformation, and strain localization, particularly within fluid-active shear zones where dissolution–reprecipitation processes accelerate structural ordering of carbon (49, 50, 52). Such localized shear-related fluid flow can produce structurally controlled graphite precipitated from preexisting, commonly organic-derived CM within veins, while preserving poorly ordered kerogen in the surrounding low-permeability siliceous matrix metamorphosed only to greenschist-facies conditions (53, 54). As the sample locality lies along the southern boundary of the regional Singhbhum Shear Zone and preserves well-developed shear fabrics, including S–C foliations, stretching lineations (Fig. 2 *B* and *D*), and L-tectonites within associated conglomerate clasts (47), the graphite-bearing hydrothermal overprint is most plausibly related to regional shear deformation. Localized fluid-assisted deformation along high-strain pathways likely promoted graphitization within veins, whereas heterogeneous strain distribution and limited permeability in the surrounding

Table 2. U-Pb secondary ion mass spectrometer data of BTDR-1 zircons

Spot	$^{207}Pb/^{206}Pb$ Age (Ma)	Age Err (Ma) 1 SE	% disc	$^{206}Pb/^{238}U$ Age (Ma)	1 SE	$^{207}Pb/^{235}U$ Age (Ma)	1 SE	% Radiogenic ^{206}Pb	Th/U	1 SD
btdr1-E1.ais	3,076	21	75	1,760	61	2,444	46	99.64	0.74	0.21
btdr1-E2.ais	3,146	41	129	1,376	95	2,232	67	99.50	0.99	0.30
btdr1-A.ais	3,195	10	40	2,283	78	2,799	36	99.81	0.51	0.15
btdr1-F.ais	3,449	4	11	3,112	51	3,321	21	99.85	0.73	0.22
btdr1-C.ais	3,471	8	3	3,357	50	3,429	21	99.77	0.67	0.19
btdr1-B.ais	3,492	7	1	3,470	42	3,484	13	99.74	0.33	0.09
btdr1-D.ais	3,498	3	3	3,397	43	3,461	15	99.71	0.49	0.14
btdr1-G.ais	3,510	5	2	3,453	44	3,489	16	99.74	0.81	0.23

For detailed analysis results, see Dataset S3.

siliceous matrix preserved the structurally disordered nature of the matrix-hosted CM.

3.3. The δ^{13}C Signature of Bhitardari CM. The different metabolic pathways of autotrophic prokaryotes fractionate carbon isotopes differently and thus signatures of the kerogenous constituents of fossil microorganisms may provide evidence of metabolic and phylogenetic affinities. For example, the kinetic isotope fractionation catalyzed by RuBisCO, the dominant CO_2-fixing enzyme of the Calvin cycle, typically produces a δ^{13}C depletion of –20 to –30‰ relative to inorganic carbon (e.g., ref. 55). The reductive citric acid cycle, used by all aerobic organisms, yields δ^{13}C fractionations of about –10‰, the reductive pentose phosphate cycle about –25‰, the reductive acetyl-CoA pathway about –35‰ δ^{13}C, and methanogenesis up to –90‰ δ^{13}C (56 and references therein). Given that the δ^{13}C of organic carbon increases by ~3‰ during greenschist-facies metamorphic graphitization (e.g., ref. 57), our data appear most consistent with preservation of biotic signatures of the acetyl-CoA and Calvin pathways. Indeed, our bulk $\delta^{13}C_{CM}$ value of –30.90‰ is consistent with the median value of Archean total organic carbon (–30.5 ± 8‰; n = 2,421) and kerogen (–33.7 ± 11.3‰; n = 556; 58). In the absence of any clear abiologic process, consistent through space and time mimicking both principal enzymic isotopic effect of the photosynthetic pathway producing consistent δ^{13}C values between –20 to –40‰ (24), we interpret our observations as a trace of early life.

3.4. Archean Greenstone-Hosted Cherts: An Archive of Early Life. The preservation of Paleoarchean kerogen within black chert associated with BIF, quartz-pebble conglomerate, volcanic tuff, quartzite, and tuffaceous phyllite (43, 47) records a volcanically active hydrothermal–sedimentary basin favorable for early microbial habitability. The association with BIF suggests deposition in ferruginous, silica-rich, anoxic marine waters where hydrothermal activity could have supplied Fe, Si, and reduced chemical species that promoted both chemogenic sedimentation and primitive microbial metabolisms (10, 59). Although uncommon, volcanism-derived zircons in cherts have been reported from Nondweni greenstone belt, Kaapvaal craton, South Africa (60). Such chert horizons are generally interpreted to form through syn-volcanic subseafloor hydrothermal circulation, where silica-rich hydrothermal fluids generated by volcanic thermal gradients mixed with seawater and precipitated silica over volcanic and sedimentary substrates (61, 62). Rapid reworking and silicification of submarine volcanic material at the sediment–water interface promoted the formation of chert layers containing volcanogenic detrital phases such as zircon, Cr-spinel, monazite, apatite (62, 63). The Bhitardari CM-bearing chert association closely resembles with Paleoarchean (ca. 3550 to 3230 Ma) Buck Reef Chert of the Barberton Greenstone Belt, where finely laminated carbonaceous cherts occur with mafic–ultramafic volcanic rocks, volcaniclastic sediments, and BIF deposited in syn-volcanic hydrothermal settings (1, 61, 64). Both successions contain alternating silica- and CM-rich laminations, intraformational chert-clast conglomerates, hydrofracturing textures, and evidence of early silicification linked to hydrothermal circulation. The strongly negative $\delta^{13}C_{CM}$ values reported from the Buck Reef Chert, together with the exclusion of Fischer–Tropsch-type abiotic synthesis, support a biological origin for the CM (65, 66).

Interlayered volcanic tuffs indicate recurrent ash input and proximity to active volcanism, providing nutrient fluxes and redox gradients conducive to microbial colonization, whereas quartzite and quartz-pebble conglomerate reflect episodic high-energy sediment influx within an evolving tectonic basin (8, 9).

Comparable CM-bearing hydrothermal cherts also occur in the ~3.4 Ga Strelley Pool Formation and the ~3.47 Ga Apex cherts of the Pilbara Craton, where carbonaceous laminations are intimately associated with volcaniclastic input, hydrothermal silicification, and putative microbial textures (6, 9, 67). Similarly, hydrothermal cherts from the Nondweni Greenstone Belt preserve volcanogenic detrital zircons within silicified basaltic sequences, linking chert deposition to active felsic volcanism (60). Archean kerogen–graphite assemblages associated with hydrothermal alteration and base-metal mineralization in the Abitibi Greenstone Belt likewise record strongly negative δ^{13}C values consistent with biogenic carbon subsequently modified by metamorphic and hydrothermal remobilization (68).

4. Conclusions

Zircons with volcanic texture recovered from the Bhitardari chert, Singhbhum craton, India, yield a ^{207}Pb/^{206}Pb age of 3497 ± 5 Ma (n = 4; MSWD = 1.2) which we take to be the age of deposition synchronous with chemical sedimentation. The Bhitardari chert represents a rare Paleoarchean archive of potential early life preserved within a volcanically active, chemogenic BIF-bearing marine system capable of sustaining early microbial habitability through redox gradients, hydrothermal nutrient supply, and rapid silica precipitation. Broad D-bands over less prominent G bands in Raman spectra from the matrix CM reveal structural disorder and possibility of indigenous kerogen preservation at low-grade thermal maturation, while strongly negative bulk $\delta^{13}C_{CM}$ values (~–30‰) support biologically mediated carbon fixation. Raman thermometry of the microbial mat-like laminations alternating with chemogenic silica yields peak metamorphic temperature of 337 ± 7 °C consistent with greenschist facies metamorphism strengthening the probability of reliable preservation of biosignatures. Together, our observations provide compelling evidence of sustenance of early life in volcanism-associated, iron- and silica-rich marine environments that constituted viable habitats for some of Earth's earliest microbial ecosystems.

5. Materials and Methods

5.1. Raman Analysis of the CM. Raman analyses were performed using a Witec Alpha300R Raman microscope at RDT (Research and Technological Development) at Ifremer, Plouzané, France. A 532 nm laser was used at 1 to 2 mW power and a spot size of 1 to 2 µm (using 100× to 50× objectives respectively). Both 600 l/mm and 1200 l/mm gratings were used, resulting in a spectral range of 0 to 4,000 or 0 to 2,000 cm^{-1} respectively. Spot analyses were obtained on rock-thin sections, with five accumulations of 60 or 120 s each. These analyses were performed by focusing the laser below the thin section surface, on carbonaceous particles that were fully enclosed by transparent quartz. This was done to avoid polishing effects caused by sample preparation. It is known that polishing causes disorder in graphitic materials (69). In order to be absolutely sure that analyses were obtained from particles below the surface, a second analytical session was performed with a Thermo Scientific DXR3 Raman microscope at Naturalis Biodiversity Center (Dutch Gemmology Laboratory–NEL). A 532 nm laser was used at 1 mW power and a spot size of 1 to 2 µm (using a 100× objective). A 1800 l/mm grating was used, resulting in a spectral range of 50 to 1,850 cm^{-1}. Spot analyses were obtained with 5× 20 s each. Specific care was taken to focus on CM particles at depths between 4 to 10 µm below the surface and to compare with CM particles in the direct vicinity at the surface. This was repeated for several CM particles in three different zones in the thin section.

The spectra were truncated to 800 to 1,900 cm^{-1} (RDT session) or 800 to 1,850 cm^{-1} (Naturalis session) and a linear background subtraction performed. Subsequently, several Raman peaks for carbonaceous material were fitted following the protocol described in ref. 70 using a Gauss-Lorentzian function. For each peak the position, intensity, full width at half-maximum, and area were calculated (see Dataset S3).

Pure crystalline graphite contains a peak at 1,580 cm^{-1} (G-peak), representing E_{2g} bond stretching of sp^2-bonded carbon. Defects in this crystal structure cause a double resonance effect leading to Raman peaks at 1,350 cm^{-1} (D1-peak) and 1,620 cm^{-1} (D2-peak). In natural carbonaceous materials, heterogeneities give rise to an additional broad peak at ca. 1,500 cm^{-1} (D3-peak) and a shoulder of the D1 peak in the 1,190 to 1,250 cm^{-1} region (D4-peak) (70). All obtained spectra were therefore decomposed in D1-, D2-, D3-, D4-, and G-peaks, following the spectral decomposition protocol of Sforna et al. (70). However, some highly crystalline graphite particles were found in a vein of sample BTDR1, for which only the D1-, D2-, and G-peak were fitted. In order to properly fit the small D1-peak in these spectra, two broad peaks at 1,250 to 1,300 cm^{-1} and 1,450 to 1,470 cm^{-1} were fitted as well.

Subsequently, the D1, D2, and G peak were used to calculate the peak intensity-based ratio $R_1 = D_1/G$, and the peak area-based ratio $R_2 = D_1/(D_1+D_2+G)$. Using the Raman-based geothermometer $T = -445*R_2+641$ (38), the peak metamorphic temperatures of the CM could then be calculated (*SI Appendix*). Calculating the average of temperatures obtained from surface and deeper analyses, we obtain high analytical precision of ±8 °C relative to the analytical uncertainty of the geothermometer reported by ref. 38.

5.2. In-Situ U-Pb Zircon Dating. Approximately 1.5 kg carbonaceous chert sample, largely devoid of secondary quartz veins, was crushed for zircon separation. U-Pb ages were measured using the *IMS*1290 ion microprobe at UCLA with a Hyperion-II ion source (71). A 3 nA O^{3-} beam focused to a ~10 μm diameter spot and accelerated at −13 kV to a sample stage held at 10 kV. Analysis followed a procedure similar to ref. 72, with a mass resolving power of ~5,000 sufficient to separate Pb masses from molecular interferences. The Pb/U relative sensitivity factor was determined using repeated measurements of age standard AS3 (1099.1 Ma; 73) and using the linear correlation between Pb^+/U^+ RSF and UO_2^+/U^+ for AS3 to correct the unknowns. Common Pb corrections were based on ^{204}Pb and assumed laboratory contamination by southern California environmental Pb (i.e., Sanudo-Wilhelmy and Flegal, 1994). Concentrations of Hf, Th, and U were estimated using standard zircon 91500 (74).

5.3. Zircon Cathodoluminescence (CL) Imaging. Cathodoluminescence (CL) imaging was performed using a Tescan Vega-3 XMU scanning electron microscope at UCLA, equipped with a 3-channel color CL detector. The sample was coated with 25 nm of carbon. A voltage of 20 kV was employed. The zircon grains have variable size and shape, varying from subhedral-prismatic (BTDR1_A-C), anhedral (BTDR1_D-E) to subrounded (grain BTDR1_F). All the grains exhibit thin oscillatory zoned outer margins and relatively homogenous cores. The zircon grains are very fine (40 to 60 μ) in size and exhibit evidence of mechanical abrasion around the surface (Fig. 4).

5.4. C- and N Isotope Analysis. Stable carbon and nitrogen isotope analyses were performed with a continuous flow mass spectrometer (Delta V+ with a conflo IV interface, Thermo Scientific, Bremen, Germany) coupled to an elemental analyzer (Flash EA 2000, Thermo Scientific, Milan, Italy) at the Pôle Spectrométrie Océan [Institut Universitaire Européen de la Mer (IUEM), Plouzané, France]. Results were expressed in standard δ notation based on international standards (Vienna Pee Dee Belemnite for $\delta^{13}C$ and atmospheric nitrogen for $\delta^{15}N$). Reference gas calibration was done using reference materials USGS 62, 63 (N) and USGS 61, 62, 63 (C).

Each 1 g sample was decarbonated using HCl (yielding roughly ≥0.95 g reflecting their highly silicic composition). Of this mass, ~30 mg was put aside and the rest was HF-treated typically leaving about 20 mg per sample. We noted a small and systematic shift between samples only decarbonated and those that were decarbonated and then treated with HF likely reflecting carbonate still trapped in chert after HCl treatment. So the most reliable data are for the HF-treated samples where the excess trapped carbonate is stripped off while the HCl treated samples yield more positive values due to the trapped carbonate in chert.

Data, Materials, and Software Availability. All study data are included in the article and/or supporting information.

ACKNOWLEDGMENTS. T.C. acknowledges the Geological Survey of India for providing her opportunity for prolonged fieldwork. She thanks Stephen J. Mojzsis and Christopher H. House for their review comments. Stephanie Zhang is thanked for her assistance with zircon separation. Enora Prado (Ifremer) and Maria El Rakwe (Ifremer) are thanked for their help with the Raman analyses. R.M. acknowledges GUtech Seed grant 2023-2025 and The Research Council of Oman BF 2023 grants for financial and infrastructural support. The ion microprobe facility at UCLA is partially supported by a grant from NSF-EAR's Instrumentation and Facilities program (2154590).

Author affiliations: [a]Secondary Ion Mass Spectrometer (SIMS) Laboratory, Geological Survey of India, Kolkata 700091, India; [b]Department of Earth, Planetary, and Space Sciences, University of California, Los Angeles, CA 90095; [c]Earth, Life, Time Group, Naturalis Biodiversity Center, Leiden 2333 CR, The Netherlands; [d]Ifremer, Research and Technological Development Unit (RDT), Plouzané F-29280, France; [e]Department of Applied Geosciences, German University of Technology in Oman, Athaibah 130, Sultanate of Oman; [f]School of Natural Sciences and Engineering, Natural Institute of Advanced Studies, Indian Institute of Science Campus, Bengaluru 560012, India; and [g]European Institute for Marine Studies, CNRS-UMR6538 Laboratoire Géo-Océan, Plouzané 29280, France

1. B. Cavalazzi, Cellular remains in a~ 3.42-billion-year-old subseafloor hydrothermal environment. *Sci. Adv.* **7**, eabf3963 (2021).
2. M. S. Dodd *et al.*, Evidence for early life in Earth's oldest hydrothermal vent precipitates. *Nature* **543**, 60–64 (2017).
3. E. J. Javaux, Challenges in evidencing the earliest traces of life. *Nature* **572**, 451–460 (2019).
4. K. Lepot, Signatures of early microbial life from the Archean (4 to 2.5 Ga) eon. *Earth Sci. Rev.* **209**, 103296 (2020).
5. J. Rouillard, M. van Zuilen, "Biosignatures and tests of biogenicity in the early rock record" in *The Archean Earth*, M. Homann *et al.*, Eds. (Elsevier, ed. 2, 2026), pp. 477–501.
6. M. D. Brasier *et al.*, Questioning the evidence for Earth's oldest fossils. *Nature* **416**, 76–81 (2002).
7. J. W. Schopf, Fossil evidence of Archaean life. *Philos. Trans. R. Soc. Lond. B Biol. Sci.* **361**, 869–885 (2006).
8. F. Westall *et al.*, Implications of a 3.472–3.333 Gyr-old subaerial microbial mat from the Barberton greenstone belt, South Africa for the UV environmental conditions on the early Earth. *Philos. Trans. R. Soc. Lond. B Biol. Sci.* **361**, 2261–2261 (2006).
9. D. Wacey, M. R. Kilburn, M. Saunders, J. Cliff, M. D. Brasier, Microfossils of sulphur-metabolizing cells in 3.4-billion-year-old rocks of Western Australia. *Nat. Geosci.* **4**, 698–702 (2011).
10. Y. Ueno, K. Yamada, N. Yoshida, S. Maruyama, Y. Isozaki, Evidence from fluid inclusions for microbial methanogenesis in the early Archaean era. *Nature* **440**, 516–519 (2006).
11. A. P. Nutman, V. C. Bennett, C. R. L. Friend, M. J. Van Kranendonk, A. R. Chivas, Rapid emergence of life shown by discovery of 3, 700-million-year-old microbial structures. *Nature* **537**, 535–538 (2016).
12. N. Noffke, D. Christian, D. Wacey, R. M. Hazen, Microbially induced sedimentary structures recording an ancient ecosystem in the ca. 3.48 billion-year-old Dresser Formation, Pilbara, Western Australia. *Astrobiology* **13**, 1103–1124 (2013).
13. H. Furnes, N. R. Banerjee, K. Muehlenbachs, H. Staudigel, M. de Wit, Early life recorded in archean pillow lavas. *Science* **304**, 578–581 (2004).
14. M. Homann *et al.*, Evidence for cavity-dwelling microbial life in 3.22 Ga tidal deposits. *Geology* **44**, 51–54 (2016).
15. A. C. Allwood, M. R. Walter, I. W. Burch, B. S. Kamber, 43 billion-year-old stromatolite reef from the Pilbara Craton of Western Australia: Ecosystem-scale insights to early life on Earth. *Precambrian Res.* **158**, 198–227 (2007).
16. D. Wacey, Stromatolites in the ∼3400 Ma Strelley pool formation, Western Australia: Examining biogenicity from the macro- to the nano-scale. *Astrobiology* **10**, 381–395 (2010).
17. R. J. Baumgartner, S. Caruso, Comment on: Carbonaceous matter in ∼3.5 Ga black bedded barite from the Dresser Formation (Pilbara Craton, Western Australia)-Insights into organic cycling on the juvenile Earth. *Precambrian Res.* **409**, 107446 (2024).
18. L. Weimann *et al.*, Carbonaceous matter in ∼3.5 Ga black bedded barite from the dresser formation (Pilbara Craton, Western Australia)-Insights into organic cycling on the juvenile Earth. *Precambrian Res.* **403**, 107321 (2024).
19. J. Kaźmierczak, B. Kremer, Pattern of cell division in ∼3.4 Ga-old microbes from South Africa. *Precambrian Res.* **331**, 105357 (2019).
20. K. Hickman-Lewis *et al.*, Metallomics in deep time and the influence of ocean chemistry on the metabolic landscapes of Earth's earliest ecosystems. *Sci. Rep.* **10**, 4965 (2020).
21. C. Heubeck, An early ecosystem of Archean tidal microbial mats (Moodies group, South Africa, ca. 3.2 Ga). *Geology* **37**, 931–934 (2009).
22. M. J. Zawaski *et al.*, Reappraisal of purported ca. 3.7 Ga stromatolites from the Isua Supracrustal Belt (West Greenland) from detailed chemical and structural analysis. *Earth Planet. Sci. Lett.* **545**, 116409 (2020).
23. M. J. Zawaski *et al.*, Marine chemical sedimentary protoliths determined for ca. 3.71 Ga calc-silicate schists and quartzites from the Isua Supracrustal Belt. *Geochim. Cosmochim. Acta* **398**, 99–118 (2025).
24. M. Schidlowski, Carbon isotopes as biogeochemical recorders of life over 3.8 Ga of Earth history: Evolution of a concept. *Precambrian Res.* **106**, 117–134 (2001).
25. Y. Ueno, H. Yurimoto, H. Yoshioka, T. Komiya, S. Maruyama, Ion microprobe analysis of graphite from ca. 3.8 Ga metasediments, Isua supracrustal belt, West Greenland: Relationship between metamorphism and carbon isotopic composition. *Geochim. Cosmochim. Acta* **66**, 1257–1268 (2002).
26. A. R. Harding, Preserved carbon isotope compositions in 3.7-billion-year-old detrital organic matter from the Isua Supracrustal Belt. *Commun. Earth Environ.* **6**, 244 (2025).

27. M. A. van Zuilen, A. Lepland, G. Arrhenius, Reassessing the evidence for the earliest traces of life. *Nature* **418**, 627–630 (2002).
28. M. A. van Zuilen *et al.*, Graphite and carbonates in the 3.8 Ga old Isua Supracrustal Belt, southern West Greenland. *Precambrian Res.* **126**, 331–348 (2003).
29. S. J. Mojzsis, Evidence for life on Earth by 3800 Myr. *Nature* **384**, 55–59 (1996).
30. C. E. Manning, S. J. Mojzsis, T. M. Harrison, Geology, age constraints, and supracrustal origin of SW Akilia Island, West Greenland. *Am. J. Sci.* **306**, 303–366 (2006).
31. K. D. McKeegan, A. B. Kudryavtsev, J. W. Schopf, Raman and ion microscopic imagery of graphitic inclusions in apatite from older than 3830 Ma Akilia supracrustal rocks, West Greenland. *Geology* **35**, 591 (2007).
32. D. Papineau *et al.*, Ancient graphite in the Eoarchean quartz–pyroxene rocks from Akilia in southern West Greenland I: Petrographic and spectroscopic characterization. *Geochim. Cosmochim. Acta* **74**, 5862–5883 (2010).
33. A. Lepland, M. A. Van Zuilen, P. Philippot, Fluid-deposited graphite and its geobiological implications in early Archean gneiss from Akilia, Greenland: Akilia graphite and its geobiological implications. *Geobiology* **9**, 2–9 (2011).
34. T. M. McCollom, J. S. Seewald, Abiotic synthesis of organic compounds in deep-sea hydrothermal environments. *ChemInform* **38**, 382–401 (2007).
35. S. McMahon, Earth's earliest and deepest purported fossils may be iron-mineralized chemical gardens. *Proc. Biol. Sci.* **286**, 20192410 (2019).
36. J. M. García-Ruiz *et al.*, Self-assembled silica-carbonate structures and detection of ancient microfossils. *Science* **302**, 1194–1197 (2003).
37. A. C. Allwood, M. T. Rosing, D. T. Flannery, J. A. Hurowitz, C. M. Heirwegh, Reassessing evidence of life in 3, 700-million-year-old rocks of Greenland. *Nature* **563**, 241–244 (2018).
38. O. Beyssac, B. Goffé, C. Chopin, J. N. Rouzaud, Raman spectra of carbonaceous material in metasediments: A new geothermometer: Raman spectroscopy of carbonaceous material. *J. Metamorph. Geol.* **20**, 859–871 (2002).
39. J. W. Schopf, A. B. Kudryavtsev, D. G. Agresti, A. D. Czaja, T. J. Wdowiak, Raman imagery: A new approach to assess the geochemical maturity and biogenicity of permineralized precambrian fossils. *Astrobiology* **5**, 333–371 (2005).
40. J. Alleon, R. E. Summons, Organic geochemical approaches to understanding early life. *Free Radic. Biol. Med.* **140**, 103–112 (2019).
41. T. Chaudhuri, Y. Wan, R. Mazumder, M. Ma, D. Liu, Evidence of enriched, Hadean mantle reservoir from 4.2-4.0 Ga zircon xenocrysts from Paleoarchean TTGs of the Singhbhum Craton, eastern India. *Sci. Rep.* **8**, 7069 (2018).
42. P. Chowdhury *et al.*, Magmatic thickening of crust in non-plate tectonic settings initiated the subaerial rise of Earth's first continents 3.3 to 3.2 billion years ago. *Proc. Natl. Acad. Sci. U.S.A.* **118**, e2105746118 (2021).
43. J. Jodder, A. Hofmann, H. Ueckermann, 3.51 Ga old felsic volcanic rocks and carbonaceous cherts from the Gorumahisani Greenstone Belt-Insights into the Palaeoarchaean record of the Singhbhum Craton, India. *Precambrian Res.* **357**, 106109 (2021).
44. J. Jodder, "The geology of the Daitari Greenstone Belt, Singhbhum Craton, India: Insights into early life 3.5 Ga ago," PhD thesis, University of Johannesburg, Johannesburg, South Africa (2021); Available from https://hdl.handle.net/10210/477262.
45. R. Mazumder *et al.*, Paleoarchean surface processes and volcanism: Insights from the eastern Iron Ore Group, Singhbhum craton, India. *Earth Sci. Rev.* **232**, 104122 (2022).
46. J. A. Dunn, A. K. Dey, *The Geology and Petrology of Eastern Singhbhum and Surrounding Areas in Memoirs of the Geological Survey of India* (Government of India Press, 1942), pp. 281–456.
47. A. Das, P. Kumar, N. Khalkho, Archaean lode gold mineralisation in Bhitar Dari area of Gorumahisani-Badampahar greenstone belt. *J. Earth Syst. Sci.* **131**, 264 (2022).
48. C. S. Palenik, L. Nasdala, R. C. Ewing, Radiation damage in zircon. *Am. Mineral.* **88**, 770–781 (2003).
49. B. Wopenka, J. D. Pasteris, Structural characterization of kerogens to granulite-facies graphite: Applicability of Raman microprobe spectroscopy. *Am. Mineralog.* **78**, 533–557 (1993).
50. P. R. Buseck, O. Beyssac, From organic matter to graphite: Graphitization. *Elements (Que.)* **10**, 421–426 (2014).
51. J. H. Oehler, Hydrothermal crystallization of silica gel. *Geol. Soc. Am. Bull.* **87**, 1143–1152 (1976).
52. Y. Kouketsu, A new approach to develop the Raman carbonaceous material geothermometer for low-grade metamorphism using peak width. *Island Arc.* **23**, 33–50 (2014).
53. D. Craw, P. Upton, Graphite reaction weakening of fault rocks, and uplift of the Annapurna Himal, Central Nepal. *Geosphere* **10**, 720–731 (2014).
54. D. Craw, D. Mackenzie, "Origin and development of a world class gold mine" in *Macraes Orogenic Gold Deposit* (Springer International Publishing, 2016), pp. 1–127.
55. C. A. Roeske, M. H. O'Leary, Carbon isotope effects on enzyme-catalyzed carboxylation of ribulose bisphosphate. *Biochemistry* **23**, 6275–6284 (1984).
56. A. L. Zerkle, Biogeochemical signatures through time as inferred from whole microbial genomes. *Am. J. Sci.* **305**, 467–502 (2005).
57. D. J. Des Marais, Isotopic evolution of the biogeochemical carbon cycle during the Proterozoic eon. *Org. Geochem.* **27**, 185–193 (1997).
58. S. S. Zeichner *et al.*, The carbon isotopic composition of Archean kerogen and its resilience through the Rock cycle. *Am. J. Sci.* **324**, 8 (2024).
59. K. O. Konhauser *et al.*, Could bacteria have formed the Precambrian banded iron formations? *Geology* **30**, 1079 (2002).
60. H. Xie *et al.*, Zircon SHRIMP dating confirms a Palaeoarchaean supracrustal terrain in the southeastern Kaapvaal Craton, Southern Africa. *Gondwana Res.* **21**, 818–828 (2012).
61. A. Hofmann, R. Bolhar, Carbonaceous cherts in the Barberton greenstone belt and their significance for the study of early life in the Archean record. *Astrobiology* **7**, 355–388 (2007).
62. A. Hofmann, C. Harris, Silica alteration zones in the Barberton greenstone belt: A window into subseafloor processes 3.5–3.3 Ga ago. *Chem. Geol.* **257**, 221–239 (2008).
63. A. Hofmann, R. Bolhar, B. Orberger, F. Foucher, Cherts of the Barberton greenstone belt, South Africa: Petrology and trace-element geochemistry of 3.5 to 3.3 Ga old silicified volcaniclastic sediments. *S. Afr. J. Geol.* **116**, 297–322 (2013).
64. D. R. Lowe, G. R. Byerly, Ironstone bodies of the Barberton greenstone belt, South Africa: Products of a Cenozoic hydrological system, not Archean hydrothermal vents! *Geol. Soc. Am. Bull.* **119**, 65–87 (2007).
65. M. M. Walsh, D. R. Lowe, "Modes of accumulation of carbonaceous matter in the early Archean: A petrographic and geochemical study of the carbonaceous cherts of the Swaziland Supergroup" in *Geologic Evolution of the Barberton Greenstone Belt, South Africa*, D. R. Lowe, G. R. Byerly, Eds. (Geological Society of America, Boulder, CO, 1999), Spec Pap 329, pp. 115–132.
66. M. A. van Zuilen, M. Chaussidon, C. Rollion-Bard, B. Marty, Carbonaceous cherts of the Barberton Greenstone Belt, South Africa: Isotopic, chemical and structural characteristics of individual microstructures. *Geochim. Cosmochim. Acta* **71**, 655–669 (2007).
67. K. Hickman-Lewis, B. Cavalazzi, F. Foucher, F. Westall, Most ancient evidence for life in the Barberton greenstone belt: Microbial mats and biofabrics of the $\sim$3.47 Ga Middle Marker horizon. *Precambrian Res.* **312**, 45–67 (2018).
68. F.-W. Wellmer, U. Berner, H. Hufnagel, H. Wehner, "Carbon isotope geochemistry of Archean carbonaceous horizons in the Timmins area" in *The Giant Kidd Creek Volcanogenic Massive Sulfide Deposit, Western Abitibi Subprovince, Canada*, M. D. Hannington, C. T. Barrie, Eds. (Society of Economic Geologists, Littleton, CO, 1999), Econ Geol Monogr 10, pp. 441–456.
69. Y. Qu, M. A. van Zuilen, A. Lepland, Hydrothermal circulation and oil migration at the root of the heterogeneous micro-structure of carbonaceous material in the 2.0 Ga Zaonega Formation, Onega Basin, Russia. *Precambrian Res.* **343**, 105705 (2020).
70. M. C. Sforna *et al.*, Evidence for arsenic metabolism and cycling by microorganisms 2.7 billion years ago. *Nat. Geosci.* **7**, 811–815 (2014).
71. M. C. Liu, K. D. McKeegan, T. M. Harrison, G. Jarzebinski, L. Vltava, The Hyperion-II radio-frequency oxygen ion source on the UCLA ims1290 ion microprobe: Beam characterization and applications in geochemistry and cosmochemistry. *Int. J. Mass Spectrom.* **424**, 1–9 (2018).
72. X. Quidelleur *et al.*, Thermal evolution and slip history of the Renbu Zedong Thrust, Southeastern Tibet. *J. Geophys. Res.* **102**, 2659–2679 (1997).
73. J. B. Paces, J. D. Miller Jr., Precise U-Pb ages of Duluth complex and related mafic intrusions, northeastern Minnesota: Geochronological insights to physical, petrogenetic, paleomagnetic, and tectonomagmatic processes associated with the 1.1 Ga Midcontinent rift system. *J. Geophys. Res.* **98**, 13997–14013 (1993).
74. M. Wiedenbeck *et al.*, Further characterisation of the 91500 zircon crystal. *Geostand. Geoanal. Res.* **28**, 9–39 (2004).